

Evolution of Defects, Morphology, and Strain during FAMAPbI₃ Perovskite Vacuum Deposition: Insights from In Situ Photoluminescence and X-ray Scattering

Vladimir Held,* Nada Mrkyvkova, Yuriy Halahovets, Peter Nádaždy, Karol Vegso, Aleš Vlk, Martin Ledinský, Matej Jergel, Sigrid Bernstorff, Jozef Keckes, Frank Schreiber, and Peter Siffalovic



Cite This: *ACS Appl. Mater. Interfaces* 2024, 16, 35723–35731



Read Online

ACCESS |



Metrics & More



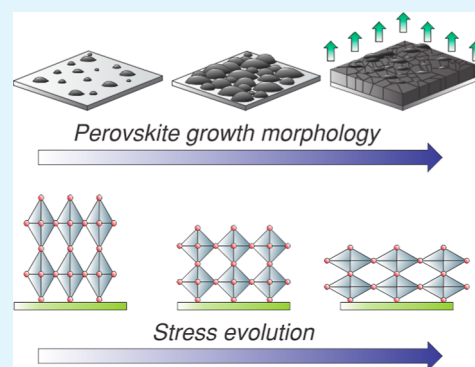
Article Recommendations



Supporting Information

ABSTRACT: At present, the power conversion efficiency of single-junction perovskite-based solar cells reaches over 26%. The further efficiency increase of perovskite-based optoelectronic devices is limited mainly by defects, causing the nonradiative recombination of charge carriers. To improve efficiency and ensure reproducible fabrication of high-quality layers, it is crucial to understand the perovskite nucleation and growth mechanism along with associated process control to reduce the defect density. In this study, we investigate the growth kinetics of a promising narrow bandgap perovskite, formamidinium methylammonium lead iodide (FAMAPbI₃), for high-performance single-junction solar cells. The temporal evolution of structural and optoelectronic properties during FAMAPbI₃ vacuum codeposition was inspected in real time by grazing-incidence wide-angle X-ray scattering and photoluminescence. Such a combination of analytical techniques unravels the evolution of intrinsic defect density and layer morphology correlated with lattice strain from the early stages of the perovskite deposition.

KEYWORDS: lead-halide perovskites, vacuum deposition, in situ characterization, defects, intrinsic stress



INTRODUCTION

Metal halide perovskites have gained significant attention as a promising material in optoelectronic technology.^{1–5} In the field of solar cells, they are perceived as competitive with or complementary to silicon-based thin films mainly due to the prospect of high power conversion efficiency, currently reaching ~26%.⁶ Moreover, the feasibility of band gap tuning extends the utilization of metal halide perovskites to multi-junction solar cells.^{7,8}

Formamidinium lead iodide (FAPbI₃) is considered the most promising material for high-performance perovskite solar cells because of the ideal band gap^{9,10} and good thermal stability.^{11,12} However, postannealing above 130 °C is required to achieve the photoactive (cubic) α -phase.^{13–15} Moreover, FAPbI₃ undergoes a spontaneous back transition from the α -phase to the nonperovskite photoinactive δ -phase at room temperature.^{16,17} Various approaches have been suggested to suppress the formation of the δ -phase and stabilize the α -phase, especially for solution-processed perovskites.^{18–22} For vacuum codeposition, the stabilization of the α -phase was achieved by the incorporation of cations with smaller ion radii into the FAPbI₃, such as cesium (Cs⁺) or methylammonium (MA⁺), while an additional annealing step to form α -phase is not required.^{23–27} Gil-Escrig et al.²³ showed that in the case of MA⁺ incorporation, the MA⁺ content in the perovskite film is

self-saturating with respect to the methylammonium iodide (MAI) deposition rate. This finding alleviates the difficulty of reliably controlling the MAI deposition rate, which depends on the impurity concentration.^{28,29}

Most research efforts in perovskite solar cells initially focused on the specific deposition conditions and finding the optimal deposition procedure. The development was mainly based on trial and error.³⁰ Nevertheless, understanding the fundamental mechanisms of crystal growth is essential for developing optimized manufacturing processes resulting in perovskite layers with minimum defects. Here, the in situ studies have a great advantage over the ex situ measurements.³¹ For example, the information obtained ex situ can be insufficient and/or potentially misleading, as the sample conditions during and after growth may differ, and certain growth phases may even be inaccessible.^{30,32,33}

In this work, we present a combined measurement of in situ photoluminescence (PL) and grazing-incidence wide-angle X-

Received: March 12, 2024

Revised: June 10, 2024

Accepted: June 12, 2024

Published: June 27, 2024



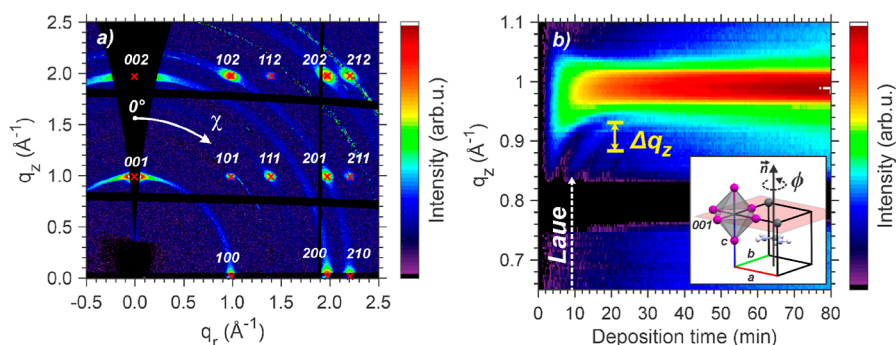


Figure 1. (a) GIWAXS pattern of the perovskite layer acquired at the end of the deposition; layer thickness ~ 62 nm. (b) Temporal evolution of the perovskite 001 diffraction peak. The white dashed arrow indicates the appearance of Laue oscillations with a satellite peak spacing Δq_z . Inset: unit cell orientation of the cubic FAPbI₃ perovskite. GIWAXS intensity in (a,b) is shown in a logarithmic scale.

ray scattering (GIWAXS), revealing the evolution of both electronic and structural properties during the vacuum codeposition of the α -FAPbI₃ perovskite stabilized by MAI. The simultaneous measurement of PL and GIWAXS enabled us to study the FAMAPbI₃ growth from the early nucleation stages up to the complete film formation, unraveling the evolution of the crystallographic structure, defect density, surface morphology, and stress. We show that the FAMAPbI₃ growth is accompanied by a nonmonotonous evolution of PL emission, which does not correlate in a simple way with the perovskite phase volume. Such behavior of PL emission has been observed in our previous work for tetragonal MAPbI₃ during vacuum codeposition³⁴ and cubic MAPbI₃ during spin coating.³⁵ The similar behavior presented here for the FAPbI₃-based perovskite suggests that it is universal for halide perovskite formation, regardless of the processing method and type of metal halide perovskites.

Moreover, the cubic crystallographic structure of α -FAPbI₃ allowed straightforward tracking of the intrinsic strain and the perovskite growth kinetics during the layer deposition. We further correlate the induced strain with the PL emission progression and relate the nonmonotonous PL character to the occurrence of defect states during perovskite growth. To the best of our knowledge, such in situ strain/stress tracking during the perovskite layer formation has not been reported yet. Additionally, the fundamental reciprocity relation between the absorption and PL emission³⁶ enabled the determination of the Urbach energy to follow the optoelectrical quality of deposited perovskite films.

EXPERIMENTAL SECTION

The FAMAPbI₃ perovskite was grown by vacuum thermal codeposition of three precursors—lead iodide (PbI₂), formamidinium iodide (FAI), and MAI. A custom-made vacuum chamber equipped with two viewports and a 360° cylindrical beryllium (Be) window was used, enabling simultaneous measurement of PL and GIWAXS during the FAMAPbI₃ growth.^{34,37} The precursors were evaporated at a base pressure of $\sim 10^{-6}$ mbar on a Si substrate (with native oxide) at room temperature. The deposition chamber was equipped with three separate QCM sensors placed near the evaporators to measure the deposition rate of each precursor. Once the rates were stable, the FAMAPbI₃ deposition started by opening the shutter located just above the sample surface. To increase the temporal resolution of the GIWAXS measurement, the entire experiment was performed at the synchrotron facility Elettra (Italy, SAXS beamline), allowing investigation of the early stages of perovskite deposition. For a detailed description of the FAMAPbI₃ vacuum deposition, experimental conditions, and setup, see the Supporting Information.

RESULTS AND DISCUSSION

First, we describe GIWAXS results to characterize the crystallographic properties of the deposited thin film. Figure 1a shows the GIWAXS reciprocal space map after background subtraction acquired at the end of the deposition process when the perovskite layer thickness was ~ 62 nm. The measured diffraction peaks indicate a preferential orientation (texture) of perovskite crystallites. We note that the grainy diffraction rings visible in the GIWAXS reciprocal map originate from the chamber Be window, thus having no connection with the grown perovskite film. Indexing the diffraction peaks using the GIXSGUI code³⁸ suggests an α -cubic perovskite crystal structure with [001] direction parallel to the substrate normal (and (001) lattice planes parallel to the substrate, see the inset in Figure 1b) while the crystallites being randomly rotated by angle ϕ around the substrate normal (n), the so-called uniaxial or $\langle 001 \rangle$ fiber texture.^{39,40} The Miller indices of each diffraction and calculated theoretical peak positions for lattice parameter $a = 6.37$ Å are marked by red crosses in Figure 1a. The value of the used lattice parameter a is comparable to the reported values for the α -FAPbI₃ perovskite.^{41–43} The observed cubic phase of the FAMAPbI₃ layer implies that the postdeposition annealing step is not required to achieve the photoactive α -phase for vacuum-deposited layers.

In the next step, we analyze the time-resolved in situ GIWAXS data. To track the temporal evolution of perovskite and precursors' PbI₂, FAI, and MAI phases, we thoroughly investigated the section of the reciprocal space within the limits $q_z = 0.65–1.1$ Å⁻¹ and $\chi = -15$ to 15° (see Figure 1a for schematic indication of χ). Here, the measured scattering intensity was integrated along the azimuthal angle χ at each q_z value. The time evolution of the integrated GIWAXS intensity during the perovskite growth is plotted in Figure 1b. We note that the blank region around $q_z \sim 0.8$ Å⁻¹ is the intermodular detector gap. Clearly, the diffraction peak at $q_z \sim 1.0$ Å⁻¹ corresponds to the FAMAPbI₃ perovskite phase.²² Diffraction peaks originating from MAI, PbI₂, and FAI are expected at $q_z \sim 0.7, 0.89,$ and 0.91 Å⁻¹, respectively.⁴⁴ However, no significant signal indicating precursors' excess in the perovskite layer was observed during the growth. The first indication of the perovskite 001 diffraction peak is resolved after ~ 2.5 min of deposition. No structural phase transition of the perovskite was observed during deposition, meaning only the cubic α -phase was found. Nevertheless, we observe additional diffraction signals at ~ 10 min of deposition, which we attribute to Laue oscillations originating from constructive interference of

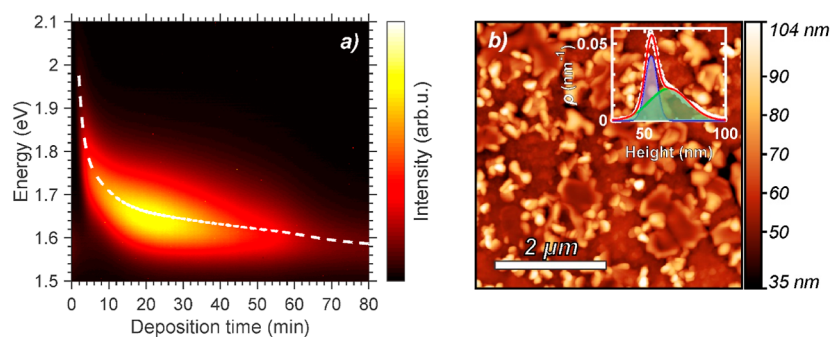


Figure 2. (a) Heat map of spectrally resolved PL measured during codeposition of FAMAPbI₃. The white dashed line indicates the spectral position of the PL peak. The collected signal intensity is colored in linear scale, and the color scale indicates the intensity increase from black to white. (b) AFM image of the final perovskite layer with height histogram in the inset.

coherently diffracting perovskite crystallites. Generally, such oscillations indicate well-grown films, demonstrating high quality in terms of both crystallinity and homogeneity.^{45,46} From the relative separation of satellite peaks Δq_z (Figure 1b), the film thickness can be estimated,⁴⁷ being ~ 13.5 nm after 20 min of deposition. Considering the average deposition rate calculated from the final average thickness of the film (~ 0.115 Å/s), the expected thickness at this time (~ 20 min) is ~ 13.8 nm. These two values of film thickness are in close agreement. Therefore, we ascribe these additional diffraction signals to the presence of a highly ordered crystalline perovskite phase.

Before exploring the GIWAXS data in more detail, we will examine the results obtained by PL measurement to establish a basis for the correlation of structural and optoelectronic properties. Figure 2a shows the heat map of PL spectra acquired during the perovskite deposition. The emission intensity is color-coded, increasing from black to yellow. The spectral position of the PL peak was obtained by fitting individual spectra by the PseudoVoigt function and is indicated by the white dashed line in Figure 2a. The PL during the perovskite growth is characterized by a nonmonotonous evolution of emission intensity and an abrupt spectral shift of the peak position. At the beginning of the deposition, the spectral position of the PL peak is found at ~ 2 eV. Afterward, it continuously red shifts to lower values up to ~ 1.58 eV at the end of the deposition, approaching a typical PL emission energy of α -FAPbI₃.^{11,23,24,48} The initial blue shift in PL emission is associated with the quantum confinement effect caused by finite-size crystallites or a limited layer thickness. At the beginning of the deposition, small islands nucleate and increase in size. We expect the diameter of the islands to be much larger than their height—similarly as observed in our previous work focused on MAPbI₃ deposition (ref 34, Figure S12) and by Parrot et al. in ref 49. Therefore, we assume the quantum confinement effect only in one dimension—in the direction perpendicular to the substrate. As the individual crystallites (or layer) grow, their height slowly increases, resulting in the red shift of the PL peak. The gradual growth of the perovskite phase is also confirmed by GIWAXS diffraction intensity increase (see Figure S4 in the Supporting Information). Additionally, the asymmetry and broadening of the PL emission peak can be observed, which can be associated with the presence of crystallites of different sizes throughout the deposition. Importantly, grain nucleation is a random process, both in time and space. Thus, we expect thickness variations in the lateral direction throughout the entire deposition. Figure 2b shows the AFM image of the final

polycrystalline film acquired after deposition, with the height distribution histogram in the inset to illustrate this effect. It can be seen that the layer consists of grains of different heights, with two characteristic values of $\sim 53 \pm 2.5$ and 65 ± 9 nm. We anticipate a similar situation during the growth. Separated grains, or regions of a continuous layer, have slightly different thicknesses and, therefore, different PL emissions, reflected in a broadening of the PL (for more details, see the Supporting Information).

The initial increase of the PL emission intensity (indicated by color in the heat map in Figure 2a) is associated with the growth of small perovskite crystallites. As more material is deposited, a larger volume of the perovskite phase emits light. Subsequently, a decrease of PL emission (starting at ~ 20 min of deposition) follows, reaching a final saturation despite the continuous growth of the perovskite phase confirmed by GIWAXS (see Figure S4). The similar nonmonotonous character of PL emission represented by an initial increase and subsequent decrease during the formation of solution-processed perovskites was reported by Wagner et al.,⁵⁰ Suchan et al.,⁵¹ and Song et al.^{52,53} Nevertheless, a complete explanation for this behavior has not yet been proposed.

Based on the results obtained by simultaneous measurement of X-ray scattering and PL during MAPbI₃ growth via solution processing³⁵ and vacuum codeposition,³⁴ we suggest the following explanation of the quenching of PL: initially, small perovskite crystallites grow up to the point when they become spatially limited by the neighboring grains (i.e., the length scale is determined by the nucleation density). The adjacent grains come into contact during coalescence, forming grain boundaries with defective states. Consequently, these defects act as recombination centers, causing the nonradiative recombination of charge carriers and, therefore, decay in the PL emission. In the case of vacuum codeposition, the growth after coalescence is maintained in the vertical direction. Therefore, we connect the PL intensity saturation with reaching the penetration limit of the excitation laser ($\lambda_{\text{exc}} = 405$ nm), which is approximately ~ 30 – 50 nm (depending on the perovskite density). All laser photons are absorbed for such perovskite thicknesses and additional deposited material will not increase the measured PL intensity. Nevertheless, no reliable evidence regarding structural growth kinetics has been provided to support this PL behavior hypothesis. Here, the cubic nature of the α -FAPbI₃-based perovskite facilitates the opportunity to study the structural evolution via intrinsic stress induced during the deposition process and correlate it directly with the optoelectronic properties.

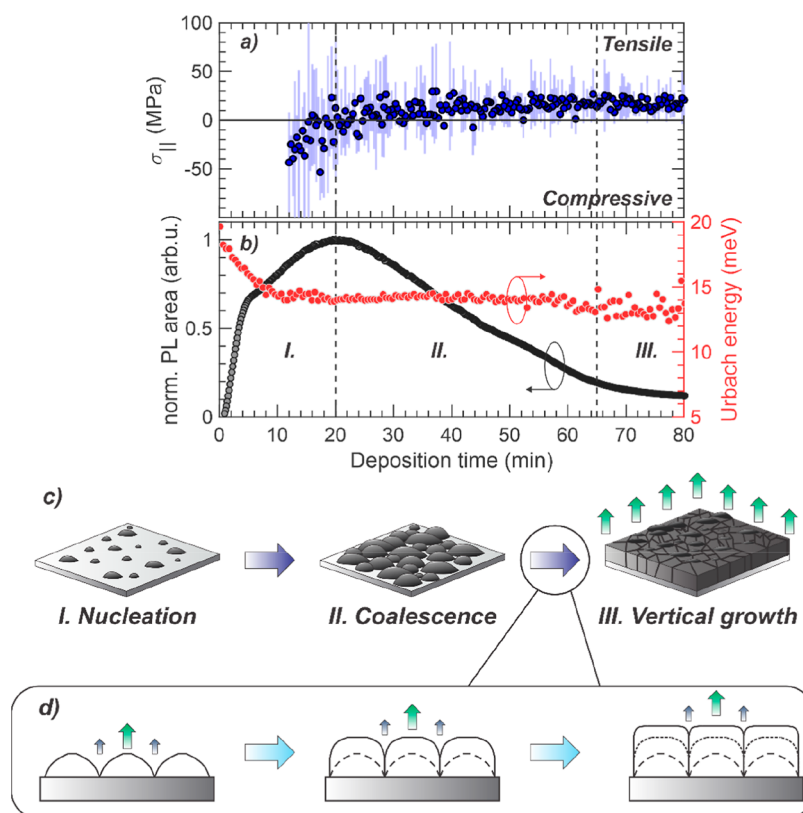


Figure 3. (a) Time evolution of intrinsic equi-biaxial in-plane stress in the FAMAPbI₃ perovskite thin film induced during the vacuum deposition. (b) Time evolution of the normalized PL peak area (black) and Urbach energy (red) calculated from PL emission. The black dashed lines in (a,b) indicate the three stages (I–III) of perovskite growth depicted in (c). (d) Illustration of the zipping process occurring between stage II and III.

Therefore, to further characterize the perovskite growth kinetics, we thoroughly analyzed the GIWAXS pattern. This allows us to track the internal X-ray elastic strains and in-plane stress developed gradually in the growing layer. The GIWAXS patterns were analyzed using the $\sin^2\psi$ method, commonly used for diffraction scans with a point detector. In the standard approach with a point detector, the sample is stepwise tilted by different angles ψ , where the angle ψ represents the angle between the thin film normal and the diffraction vector, while the lattice spacing of crystallographic planes is measured by performing a $2\theta/\theta$ scan at every tilt.⁴⁰ In the case of a 2D detector, each point along the Debye–Scherrer ring corresponds to various diffraction vector orientations, and the diffraction angles vary across the ring. For thin films, the Debye–Scherrer rings are deformed to an elliptical shape due to the internal equi-biaxial stress, and the dependence of the diffraction peak position q on $\sin^2\psi$ follows a linear relation. Subsequently, the magnitude and type (compressive or tensile) of the residual stress can be deduced from the slope of this linear dependence.⁴⁰ We note that for diffraction geometry presented in this work (utilizing the 2D detector), the polar angle χ indicated in Figure 1a represents the angle ψ . Therefore, we depict the measured lattice spacing as a function of the angle χ instead of ψ (Figure S8 in the Supporting Information). Since we utilize a 2D detector and noncoplanar geometry, the $\sin^2\chi$ plot can be obtained directly from a single acquisition (GIWAXS pattern) without the necessity of sample tilt. Specifically, due to the uniaxial texture of perovskite crystallites, see Figure 1a, we notice various diffraction spots at distinct χ angles instead of the typical Debye–Scherrer rings.⁵⁴ Because of the uniaxial texture, we can also assume the equi-

biaxial in-plane stress in the perovskite layer.^{40,55} Consequently, the stress tensor is fully characterized by only two nonzero diagonal in-plane stress components $\sigma_{xx} = \sigma_{yy} = \sigma_{||}$ ^{40,55} for the cubic structure. The residual stress is then calculated from the dependence of the lattice parameter on $\sin^2\chi$ as follows⁵⁴

$$\frac{\partial a}{\partial \sin^2\chi} = \frac{1}{2}\sigma_{||}S_2a_0 \quad (1)$$

Here, the term $\partial a/\partial \sin^2\chi$ is the slope of the linear dependence of the cubic lattice parameter a on $\sin^2\chi$, $\sigma_{||}$ represents the equi-biaxial in-plane stress magnitude, S_2 denotes the X-ray elastic constant, and a_0 is the unstrained lattice parameter. The linear dependence of the lattice a parameter on $\sin^2\chi$ was calculated, taking into account various diffraction peaks at different polar angles. Specifically, the 102, 120, and 210 peaks have been used for analysis (see Figure 1a), since these peaks are the most intense and span the χ range from ~ 26 to 90° . For more details on the stress evaluation, see the Supporting Information. Figure 3a illustrates the in-situ-measured evolution of in-plane stress within the layer during the perovskite deposition. Negative values of stress ($\sigma_{||} < 0$) indicate a compressive, and the positive values ($\sigma_{||} > 0$) correspond to a tensile in-plane stress. We note that the in situ stress analysis was possible from ~ 12 min of the deposition since the intensity of particular diffraction peaks used was insufficient in the earlier deposition stages. At the beginning of the perovskite deposition, the observed shift in diffraction peak positions indicates compressive stress. Subsequently, at ~ 20 min of deposition, we detect the transition from the

compressive to tensile stress state. Following this transition, the stress state remains tensile, reaching ~ 20 MPa at the end of the deposition. This value falls into the interval of the previously reported stress values of ~ 10 – 75 MPa for metal halide perovskites prepared by solution processing.^{56–58} Since, to the best of our knowledge, the ex situ residual stress analysis of halide perovskite layers fabricated via vacuum codeposition has not been reported before, there is no direct comparison with the literature.

The evolution of internal in-plane stress during the Volmer–Weber growth of polycrystalline films (typical for vacuum-grown perovskites) has been extensively studied. The theory was provided in the work of Abermann and Hoffmann^{59,60} and has later undergone some refinements.^{61–65} We will adopt this theory to correlate the stress evolution during perovskite growth with the structural changes. Generally, three stages of growth are distinguished, depicted in Figure 3c. In the first stage (I), when small islands nucleate, compressive stress is developed. The compressive stress is achieved by two simultaneous mechanisms. The first is related to the internal elastic strain in growing islands, as the lattice spacing in a small isolated crystallite is smaller than in a bulk crystal.

The second one is associated with the islands' strong attachment or "freezing" to the substrate having a different lattice parameter than if only Laplace pressure is considered, resulting in compressive stress in islands.^{63,64} The next stage (II) is associated with the coalescence of particular islands. As the islands grow, they cover bare substrate surfaces in between, up to the point when they start to touch each other, resulting in layer formation. Free surfaces where the islands are in contact fuse together, forming grain boundaries and thus reducing the surface energy.^{66,67} As atoms from adjacent grains are mutually attracted, tensile stress is developed.⁶⁵ Therefore, the transition from compressive to tensile stress is regarded as the onset of coalescence. Generally, the island nucleation is temporally and spatially random. There is a distribution in the islands' size and mutual distance. Thus, the coalescence of all islands is not instantaneous, which results in a gradual increase in tensile stress.⁶⁸ Moreover, a continuous increase in tensile stress can be explained by the so-called zipping of adjacent grains at the contact point and the continuous growth of the grain boundary.^{65,67,68} The zipping process is schematically depicted in Figure 3d. At the point when the height of the grain boundary is comparable with the thickness of the layer, the tensile stress saturates.⁶⁷ The final stage (III) is connected with vertical growth when the perovskite layer is fully developed with its characteristic roughness. The stress state remains tensile in the case of FAMAPbI₃, as in the case of other low-mobility materials.⁶⁵ Many studies have shown that the presence of tensile stress is detrimental to the device performance.^{56,69} Adding a dedicated interlayer could reduce a lattice mismatch between such an interlayer and the perovskite film. This could lead to a different growth mode, preferably layer-by-layer, and subsequently reduce the tensile stress. However, such an interlayer must fulfill other stringent criteria, e.g., proper band alignment for charge separation, high conductivity, and ease of fabrication.

To further correlate structural and optoelectronic properties, the evolution of the PL emission intensity (in the form of the normalized area under the PL peak, indicated by black color; the PL normalization was performed to the maximum PL intensity value reached during the deposition) temporally aligned with the stress evolution is shown in Figure 3b.

Comparing the PL intensity and stress evolution, we observe agreement with the PL quenching hypothesis and structurally induced stress. Specifically, when the onset of coalescence is expected, evident from the stress-state transition/relaxation, the PL intensity maximum is reached. Subsequently, the PL decay follows as the grain boundaries are formed. The gradual decrease in the PL emission intensity is attributed to the fact that the coalescence does not occur simultaneously for all grains. In addition, the grain boundaries grow progressively through the zipping process (see Figure 3d). Thus, more defect states are formed continuously as the contact area of adjacent islands or grain boundaries enlarges. We connect the electronic nature of these defects produced at grain boundaries to deep defect states, as they cause the steady-state PL decay through (Shockley–Reed–Hall effect) nonradiative recombination.⁷⁰ In the context of the potential solar cell performance, we can deduce the photovoltaic open circuit voltage (V_{OC}) losses from the nonradiative recombination due to grain boundary formation.³⁵ Since we studied only the relative PL intensity changes, we estimate the nonradiative V_{OC} losses from the ratio of the PL peak area at the deposition end to the maximal area of the PL peak (see the Supporting Information). The acquired $\Delta V_{OC}^{non-rad}$ is reaching the value of 76 mV at the end of the deposition. It should be noted that this value represents a minimal estimate (lower limit) of $\Delta V_{OC}^{non-rad}$, as the PL intensity renormalized to the perovskite volume should be used for the calculation. Since the thickness of the layer (and also the substrate coverage) at PL maximum and PL saturation point is different, we would expect a more significant PL intensity decrease when considering the perovskite phase volume.

Additionally, the obtained PL spectra offer a direct means of determining the Urbach energy (E_U). This parameter is widely used for evaluating the optoelectronic performance potential of semiconductors. E_U reflects lattice disorder caused by various defects (vacancies, dislocations, impurities, etc.) or thermal fluctuations, creating shallow and deep states within the band gap.^{71,72} Therefore, any change in the crystallographic structure due to the impurities or stoichiometry mismatch would influence the Urbach energy. Lower values of E_U indicate a sharper absorption/emission edge, implying less structural disorder and, consequently, higher material quality. Here, the E_U was evaluated from the exponential decay of the absorption edge, calculated from the PL spectra, in the range of 1.45–1.7 eV.⁷⁰ For more details on the E_U theory and calculations, see the Supporting Information. The evolution of the Urbach energy during perovskite growth is depicted in Figure 3b (indicated by red color), showing higher values at the beginning of the FAMAPbI₃ growth and subsequent stabilization at ~ 14 meV. The initially increased value of E_U can be associated with the nucleation of crystallites of different sizes, causing the broadening of the PL peak, which results in a less sharp absorption edge. Therefore, a connection of Urbach energy with lattice disorder evolution cannot be applied at this stage, as the E_U values originate from the layer morphology reflected in the PL peak broadening. Later on, the PL broadening due to different sizes is not as pronounced, and the absorption edge reflects the lattice disorder. The subsequent stabilization of E_U at ~ 14 meV occurs before the island coalescence onset and does not change significantly throughout the deposition. The scattering of the Urbach energy values around the 14 meV level at the very end of deposition is caused by the low PL intensity and fitting error of the

absorbance spectra (see Figure S13 in the Supporting Information). The saturated value of E_U agrees well with the reported Urbach energies of metal halide perovskites.^{70–72} Such steady progression of E_U derived from PL emission indicates that the overall material quality—in terms of the shallow defect states in the band gap—remains constant. Thus, the PL quenching is attributed to the formation of the grain boundaries. It is important to note that the defects located at grain boundaries do not exhibit efficient PL (in fact, they quench the PL emission). As a result, the sensitivity to these states is limited, with the Urbach energy being more sensitive to the bulk properties of the perovskite material.

CONCLUSIONS

In conclusion, we have investigated the growth of the FAMAPbI₃ perovskite from the vapor phase during the vacuum codeposition process. The formation of the α -phase of FAPbI₃ was achieved by evaporation of supplementary MAI to stabilize the cubic structure without requiring an additional annealing step. To characterize the growth process and probe the structural and optoelectronic properties in real time, we employed simultaneous measurements of GIWAXS and PL. The high quality of perovskite thin films was confirmed by the presence of Laue oscillations developed in diffraction patterns during the deposition. We observed that the formation of the FAMAPbI₃ perovskite is characterized by an extensive PL peak position shift due to the crystallite growth and by the nonmonotonous character of PL emission intensity. Furthermore, we tracked the intrinsic stress development during deposition. The evolution of the intrinsic stress typical for Volmer–Weber-type growth offered exceptional insights into the layer formation process. Especially, the observed transition from the compressive to tensile stress confirmed the PL quenching caused by the nonradiative recombination at grain boundaries. We show that the PL evolution during the FAMAPbI₃ vacuum deposition is similar to MAPbI₃ prepared by vacuum deposition,³⁴ as well as by solution-based deposition.^{35,51–53} We suggest that such behavior is universal for the formation of polycrystalline metal halide perovskites. However, further work is required to fully comprehend the process of perovskite growth and its implications on optoelectronic properties, particularly for vapor-deposited perovskites. We demonstrate that such a combined in situ study might be a powerful tool for a broader understanding of the perovskite growth process, stress development, and further exploration of possible defect passivation techniques.

ASSOCIATED CONTENT

Supporting Information

The Supporting Information is available free of charge at <https://pubs.acs.org/doi/10.1021/acsami.4c04095>.

Detailed description of the FAMAPbI₃ vacuum deposition, experimental conditions, and setup; details on the GIWAXS measurements and analysis, including stress analysis; analysis of the measured PL spectra and Urbach energy calculation; and perovskite layer thickness determination by AFM measurements (PDF)

AUTHOR INFORMATION

Corresponding Author

Vladimir Held – *Institute of Physics, Slovak Academy of Sciences, Bratislava 845 11, Slovakia*; orcid.org/0000-0003-2210-8285; Email: vladimir.held@savba.sk

Authors

Nada Mrkyvkova – *Institute of Physics, Slovak Academy of Sciences, Bratislava 845 11, Slovakia*; *Center for Advanced Materials Application, Slovak Academy of Sciences, Bratislava 845 11, Slovakia*; orcid.org/0000-0002-2619-0872

Yuriy Halahovets – *Institute of Physics, Slovak Academy of Sciences, Bratislava 845 11, Slovakia*

Peter Nádaždy – *Institute of Physics, Slovak Academy of Sciences, Bratislava 845 11, Slovakia*; *Institute of Electrical Engineering, Slovak Academy of Sciences, Bratislava 845 11, Slovakia*

Karol Vegso – *Institute of Physics, Slovak Academy of Sciences, Bratislava 845 11, Slovakia*; *Center for Advanced Materials Application, Slovak Academy of Sciences, Bratislava 845 11, Slovakia*

Aleš Vlk – *Laboratory of Thin Films, Institute of Physics, Prague 162 00, Czech Republic*; orcid.org/0000-0003-2866-7133

Martin Ledinský – *Laboratory of Thin Films, Institute of Physics, Prague 162 00, Czech Republic*; orcid.org/0000-0002-6586-5473

Matej Jergel – *Institute of Physics, Slovak Academy of Sciences, Bratislava 845 11, Slovakia*; *Center for Advanced Materials Application, Slovak Academy of Sciences, Bratislava 845 11, Slovakia*; orcid.org/0000-0002-4482-7881

Sigrid Bernstorff – *Elettra-Sincrotrone Trieste S. C.p.A., Trieste 34149, Italy*; orcid.org/0000-0001-6451-5159

Jozef Keckes – *Department of Materials Science, Montanuniversität Leoben, Leoben A-8700, Austria*

Frank Schreiber – *Institute of Applied Physics, University of Tübingen, Tübingen 72076, Germany*; orcid.org/0000-0003-3659-6718

Peter Siffalovic – *Institute of Physics, Slovak Academy of Sciences, Bratislava 845 11, Slovakia*; *Center for Advanced Materials Application, Slovak Academy of Sciences, Bratislava 845 11, Slovakia*; orcid.org/0000-0002-9807-0810

Complete contact information is available at: <https://pubs.acs.org/10.1021/acsami.4c04095>

Notes

The authors declare no competing financial interest.

ACKNOWLEDGMENTS

We acknowledge the financial support of projects APVV-21-0297, APVV-20-0111, SK-CZ-RD-21-0043, SK-AT-20-0006, and 2023/727/PVKSC (RS-2023-00266946). This work was performed during the implementation of the project Research of New Materials by Methods of Advanced Diagnostics, ITMS 313011U400, and the project Building-up Centre for Advanced Materials Application of the Slovak Academy of Sciences, ITMS2014+: 313021T081, supported by the Research and Innovation Operational Programme funded by the ERDF and by the IMPULS programme of the Slovak Academy of Sciences on the basis of contract no. IM-2023-82.

The authors also acknowledge the support by the BMBF and DFG, projects LUASK 22202, GACR 24-11652S and PVKSC 9F23003, and the use of the CzechNanoLab research infrastructure supported by the MEYS (LM2023051).

REFERENCES

- (1) Xing, G.; Mathews, N.; Lim, S. S.; Yantara, N.; Liu, X.; Sabba, D.; Grätzel, M.; Mhaisalkar, S.; Sum, T. C. Low-temperature solution-processed wavelength-tunable perovskites for lasing. *Nat. Mater.* **2014**, *13* (5), 476–480.
- (2) Tan, Z.; Moghaddam, R. S.; Lai, M. L.; Docampo, P.; Higler, R.; Deschler, F.; Price, M.; Sadhanala, A.; Pazos, L. M.; Credgington, D.; et al. Bright light-emitting diodes based on organometal halide perovskite. *Nat. Nanotechnol.* **2014**, *9* (9), 687–692.
- (3) Dou, L.; Yang, Y.; You, J.; Hong, Z.; Chang, W. H.; Li, G.; Yang, Y. Solution-processed hybrid perovskite photodetectors with high detection. *Nat. Commun.* **2014**, *5* (1), 5404.
- (4) Chen, Y.-S.; Manser, J. S.; Kamat, P. V. All Solution-Processed Lead Halide Perovskite-BiVO₄ Tandem Assembly for Photolytic Solar Fuels Production. *J. Am. Chem. Soc.* **2015**, *137* (2), 974–981.
- (5) Kojima, A.; Teshima, K.; Shirai, Y.; Miyasaka, T. Organometal Halide Perovskites as Visible-Light Sensitizers for Photovoltaic Cells. *J. Am. Chem. Soc.* **2009**, *131* (17), 6050–6051.
- (6) Green, M. A.; Dunlop, E. D.; Siefert, G.; Yoshita, M.; Kopidakis, N.; Bothe, K.; Hao, X. Solar cell efficiency tables (Version 61). *Prog. Photovoltaics Res. Appl.* **2023**, *31* (1), 3–16.
- (7) Eperon, G. E.; Hörantner, M. T.; Snaith, H. J. Metal halide perovskite tandem and multiple-junction photovoltaics. *Nat. Rev. Chem.* **2017**, *1*, 0095.
- (8) Noh, J. H.; Im, S. H.; Heo, J. H.; Mandal, T. N.; Seok, S. I. Chemical Management for Colorful, Efficient, and Stable Inorganic–Organic Hybrid Nanostructured Solar Cells. *Nano Lett.* **2013**, *13*, 1764–1769.
- (9) Rühle, S. Tabulated values of the Shockley-Queisser limit for single junction solar cells. *Sol. Energy* **2016**, *130*, 139–147.
- (10) Koh, T. M.; Fu, K.; Fang, Y.; Chen, S.; Sum, T. C.; Mathews, N.; Mhaisalkar, S. G.; Boix, P. P.; Baikie, T. Formamidinium-Containing Metal-Halide: An Alternative Material for Near-IR Absorption Perovskite Solar Cells. *J. Phys. Chem. C* **2014**, *118*, 16458–16462.
- (11) Ma, F.; Li, J.; Li, W.; Lin, N.; Wang, L.; Qiao, J. Stable α/δ phase junction of formamidinium lead iodide perovskites for enhanced near-infrared emission. *Chem. Sci.* **2017**, *8* (1), 800–805.
- (12) Juarez-Perez, E. J.; Ono, L. K.; Qi, Y. Thermal degradation of formamidinium based lead halide perovskites into: Sym-triazine and hydrogen cyanide observed by coupled thermogravimetry-mass spectrometry analysis. *J. Mater. Chem. A* **2019**, *7* (28), 16912–16919.
- (13) Borchert, J.; Milot, R. L.; Patel, J. B.; Davies, C. L.; Wright, A. D.; Martínez Maestro, L.; Snaith, H. J.; Herz, L. M.; Johnston, M. B. Large-Area, Highly Uniform Evaporated Formamidinium Lead Triiodide Thin Films for Solar Cells. *ACS Energy Lett.* **2017**, *2* (12), 2799–2804.
- (14) Stoumpos, C. C.; Malliakas, C. D.; Kanatzidis, M. G. Semiconducting Tin and Lead Iodide Perovskites with Organic Cations: Phase Transitions, High Mobilities, and Near-Infrared Photoluminescent Properties. *Inorg. Chem.* **2013**, *52*, 9019–9038.
- (15) Binek, A.; Hanusch, F. C.; Docampo, P.; Bein, T. Stabilization of the trigonal high-temperature phase of formamidinium lead iodide. *J. Phys. Chem. Lett.* **2015**, *6* (7), 1249–1253.
- (16) Gu, L.; Zhang, D.; Kam, M.; Zhang, Q.; Poddar, S.; Fu, Y.; Mo, X.; Fan, Z. Significantly improved black phase stability of FAPbI₃ nanowires via spatially confined vapor phase growth in nanoporous templates. *Nanoscale* **2018**, *10* (32), 15164–15172.
- (17) Zheng, X.; Wu, C.; Jha, S. K.; Li, Z.; Zhu, K.; Priya, S. Improved Phase Stability of Formamidinium Lead Triiodide Perovskite by Strain Relaxation. *ACS Energy Lett.* **2016**, *1*, 1014–1020.
- (18) Fan, Y.; Meng, H.; Wang, L.; Pang, S. Review of Stability Enhancement for Formamidinium-Based Perovskites. *Sol. RRL* **2019**, *3* (9), 1900215.
- (19) Lyu, M.; Park, N. G. Effect of Additives AX (A = FA, MA, Cs, Rb, NH₄, X = Cl, Br, I) in FAPbI₃ on Photovoltaic Parameters of Perovskite Solar Cells. *Sol. RRL* **2020**, *4* (10), 1–10.
- (20) Lee, J. W.; Dai, Z.; Lee, C.; Lee, H. M.; Han, T. H.; De Marco, N.; Lin, O.; Choi, C. S.; Dunn, B.; Koh, J.; et al. Tuning Molecular Interactions for Highly Reproducible and Efficient Formamidinium Perovskite Solar Cells via Adduct Approach. *J. Am. Chem. Soc.* **2018**, *140* (20), 6317–6324.
- (21) Kim, M.; Kim, G. H.; Lee, T. K.; Choi, I. W.; Choi, H. W.; Jo, Y.; Yoon, Y. J.; Kim, J. W.; Lee, J.; Huh, D.; et al. Methylammonium Chloride Induces Intermediate Phase Stabilization for Efficient Perovskite Solar Cells. *Joule* **2019**, *3* (9), 2179–2192.
- (22) Slimi, B.; Mollar, M.; Assaker, I. B.; Kriaa, I.; Chtourou, R.; Marí, B. Perovskite FA1-xMAxPbI₃ for Solar Cells: Films Formation and Properties. *Energy Procedia* **2016**, *102*, 87–95.
- (23) Gil-Escrig, L.; Dreessen, C.; Kaya, I. C.; Kim, B. S.; Palazon, F.; Sessolo, M.; Bolink, H. J. Efficient Vacuum-Deposited Perovskite Solar Cells with Stable Cubic FA_{1-x}MA_xPbI₃. *ACS Energy Lett.* **2020**, *5* (9), 3053–3061.
- (24) Roß, M.; Severin, S.; Stutz, M. B.; Wagner, P.; Köbler, H.; Favin-Lévêque, M.; Al-Ashouri, A.; Korb, P.; Tockhorn, P.; Abate, A.; et al. Co-Evaporated Formamidinium Lead Iodide Based Perovskites with 1000 h Constant Stability for Fully Textured Monolithic Perovskite/Silicon Tandem Solar Cells. *Adv. Energy Mater.* **2021**, *11* (35), 2101460.
- (25) Gil-Escrig, L.; Momblona, C.; La-Placa, M. G.; Boix, P. P.; Sessolo, M.; Bolink, H. J. Vacuum Deposited Triple-Cation Mixed-Halide Perovskite Solar Cells. *Adv. Energy Mater.* **2018**, *8* (14), 1703506.
- (26) Gil-Escrig, L.; Dreessen, C.; Palazon, F.; Hawash, Z.; Moons, E.; Albrecht, S.; Sessolo, M.; Bolink, H. J. Efficient Wide-Bandgap Mixed-Cation and Mixed-Halide Perovskite Solar Cells by Vacuum Deposition. *ACS Energy Lett.* **2021**, *6* (2), 827–836.
- (27) Chiang, Y.-H.; Anaya, M.; Stranks, S. D. Multi-source vacuum deposition of methylammonium-free perovskite solar cells. *ACS Energy Lett.* **2020**, *5*, 2498–2504.
- (28) Borchert, J.; Levchuk, I.; Snoek, L. C.; Rothmann, M. U.; Haver, R.; Snaith, H. J.; Brabec, C. J.; Herz, L. M.; Johnston, M. B. Impurity Tracking Enables Enhanced Control and Reproducibility of Hybrid Perovskite Vapor Deposition. *ACS Appl. Mater. Interfaces* **2019**, *11* (32), 28851–28857.
- (29) Zaroni, K. P. S.; Martínez-Goyeneche, L.; Dreessen, C.; Sessolo, M.; Bolink, H. J. Photovoltaic Devices Using Sublimed Methylammonium Lead Iodide Perovskites: Long-Term Reproducible Processing. *Sol. RRL* **2023**, *7* (7), 2201073.
- (30) Miyadera, T.; Shibata, Y.; Koganezawa, T.; Murakami, T. N.; Sugita, T.; Tanigaki, N.; Chikamatsu, M. Crystallization Dynamics of Organolead Halide Perovskite by Real-Time X-ray Diffraction. *Nano Lett.* **2015**, *15* (8), 5630–5634.
- (31) Peng, J.; Xu, Y.; Yao, F.; Huang, H.; Li, R.; Lin, Q. Ion-exchange-induced slow crystallization of 2D-3D perovskite thick junctions for X-ray detection and imaging. *Matter* **2022**, *5* (7), 2251–2264.
- (32) Hu, Q.; Zhao, L.; Wu, J.; Gao, K.; Luo, D.; Jiang, Y.; Zhang, Z.; Zhu, C.; Schaible, E.; Hexemer, A.; et al. In situ dynamic observations of perovskite crystallisation and microstructure evolution intermediated from [PbI₆]⁴⁻ cage nanoparticles. *Nat. Commun.* **2017**, *8* (1), 15688.
- (33) Wang, H.; Xu, W.; Wei, Q.; Peng, S.; Shang, Y.; Jiang, X.; Yu, D.; Wang, K.; Pu, R.; Zhao, C.; et al. In-situ growth of low-dimensional perovskite-based insular nanocrystals for highly efficient light emitting diodes. *Light: Sci. Appl.* **2023**, *12* (1), 62.
- (34) Held, V.; Mrkyvkova, N.; Nádaždy, P.; Vegso, K.; Vlk, A.; Ledinský, M.; Jergel, M.; Chumakov, A.; Roth, S. V.; Schreiber, F.; et al. Evolution of Structure and Optoelectronic Properties during

- Halide Perovskite Vapor Deposition. *J. Phys. Chem. Lett.* **2022**, *13* (51), 11905–11912.
- (35) Mrkyvkova, N.; Held, V.; Nádaždy, P.; Subair, R.; Majkova, E.; Jergel, M.; Vlk, A.; Ledinsky, M.; Kotlár, M.; Tian, J.; et al. Combined in Situ Photoluminescence and X-ray Scattering Reveals Defect Formation in Lead-Halide Perovskite Films. *J. Phys. Chem. Lett.* **2021**, *12* (41), 10156–10162.
- (36) Barugkin, C.; Cong, J.; Duong, T.; Rahman, S.; Nguyen, H. T.; Macdonald, D.; White, T. P.; Catchpole, K. R. Ultralow absorption coefficient and temperature dependence of radiative recombination of CH₃NH₃PbI₃ perovskite from photoluminescence. *J. Phys. Chem. Lett.* **2015**, *6* (5), 767–772.
- (37) Ritley, K. A.; Krause, B.; Schreiber, F.; Dosch, H. A portable ultrahigh vacuum organic molecular beam deposition system for in situ x-ray diffraction measurements. *Rev. Sci. Instrum.* **2001**, *72* (2), 1453–1457.
- (38) Jiang, Z. GIXSGUI: A MATLAB toolbox for grazing-incidence X-ray scattering data visualization and reduction, and indexing of buried three-dimensional periodic nanostructured films. *J. Appl. Crystallogr.* **2015**, *48*, 917–926.
- (39) Abadias, G.; Chason, E.; Keckes, J.; Sebastiani, M.; Thompson, G. B.; Barthel, E.; Doll, G. L.; Murray, C. E.; Stoessel, C. H.; Martinu, L. Review Article: Stress in thin films and coatings: Current status, challenges, and prospects. *J. Vac. Sci. Technol., A* **2018**, *36* (2), 020801.
- (40) Birkholz, M.; Fewster, P. F.; Genzel, C. *Thin Film Analysis by X-ray Diffraction*, 2006.
- (41) Weller, M. T.; Weber, O. J.; Frost, J. M.; Walsh, A. Cubic Perovskite Structure of Black Formamidinium Lead Iodide, α -[HC(NH₂)₂]PbI₃, at 298 K. *J. Phys. Chem. Lett.* **2015**, *6* (16), 3209–3212.
- (42) Frost, J. M.; Butler, K. T.; Brivio, F.; Hendon, C. H.; Van Schilfgaarde, M.; Walsh, A. Atomistic origins of high-performance in hybrid halide perovskite solar cells. *Nano Lett.* **2014**, *14* (5), 2584–2590.
- (43) Walsh, A.; Brivio, F.; Frost, J. M. *WMD-group/hybrid-perovskites: Collection 1*, 2019.
- (44) Petrov, A. A.; Goodilin, E. A.; Tarasov, A. B.; Lazarenko, V. A.; Dorovatovskii, P. V.; Khrustalev, V. N. Formamidinium iodide: Crystal structure and phase transitions. *Acta Crystallogr., Sect. E: Crystallogr. Commun.* **2017**, *73*, 569–572.
- (45) Miller, A. M.; Lemon, M.; Choffel, M. A.; Rich, S. R.; Harvel, F.; Johnson, D. C. Extracting information from X-ray diffraction patterns containing Laue oscillations. *Zeitschrift für Naturforsch - Sect B J. Chem. Sci.* **2022**, *77* (4–5), 313–322.
- (46) Miyadera, T.; Auchi, Y.; Yamamoto, K.; Ohashi, N.; Koganezawa, T.; Yaguchi, H.; Yoshida, Y.; Chikamatsu, M. Insights into Microscopic Crystal Growth Dynamics of CH₃NH₃PbI₃ under a Laser Deposition Process Revealed by in Situ X-ray Diffraction. *ACS Appl. Mater. Interfaces* **2021**, *13* (19), 22559–22566.
- (47) Grelet, E.; Dardel, S.; Bock, H.; Goldmann, M.; Lacaze, E.; Nallet, F. Morphology of open films of discotic hexagonal columnar liquid crystals as probed by grazing incidence X-ray diffraction. *Eur. Phys. J. E* **2010**, *31* (4), 343–349.
- (48) Yoo, J. J.; Seo, G.; Chua, M. R.; Park, T. G.; Lu, Y.; Rotermund, F.; Kim, Y. K.; Moon, C. S.; Jeon, N. J.; Correa-Baena, J. P.; et al. Efficient perovskite solar cells via improved carrier management. *Nature* **2021**, *590* (7847), 587–593.
- (49) Parrott, E. S.; Patel, J. B.; Haghighirad, A. A.; Snaith, H. J.; Johnston, M. B.; Herz, L. M. Growth modes and quantum confinement in ultrathin vapour-deposited MAPbI₃ films. *Nanoscale* **2019**, *11* (30), 14276–14284.
- (50) Wagner, L.; Mundt, L. E.; Mathiazhagan, G.; Mundus, M.; Schubert, M. C.; Mastroianni, S.; Würfel, U.; Hinsch, A.; Glunz, S. W. Distinguishing crystallization stages and their influence on quantum efficiency during perovskite solar cell formation in real-time. *Sci. Rep.* **2017**, *7* (1), 14899.
- (51) Suchan, K.; Just, J.; Becker, P.; Unger, E. L.; Unold, T. Optical in situ monitoring during the synthesis of halide perovskite solar cells reveals formation kinetics and evolution of optoelectronic properties †. *J. Mater. Chem. A* **2020**, *8*, 10439–10449.
- (52) Song, T.-B.; Yuan, Z.; Babbe, F.; Nenon, D. P.; Aydin, E.; De Wolf, S.; Sutter-Fella, C. M. Dynamics of Antisolvent Processed Hybrid Metal Halide Perovskites Studied by In Situ Photoluminescence and Its Influence on Optoelectronic Properties. *ACS Appl. Energy Mater.* **2020**, *3* (3), 2386–2393.
- (53) Song, T.-B.; Yuan, Z.; Mori, M.; Motiwala, F.; Segev, G.; Masquelier, E.; Stan, C. V.; Slack, J. L.; Tamura, N.; Sutter-Fella, C. M. Revealing the Dynamics of Hybrid Metal Halide Perovskite Formation via Multimodal In Situ Probes. *Adv. Funct. Mater.* **2019**, *30*, 1908337.
- (54) Stefanelli, M.; Todt, J.; Riedl, A.; Ecker, W.; Müller, T.; Daniel, R.; Burghammer, M.; Keckes, J. X-ray analysis of residual stress gradients in TiN coatings by a Laplace space approach and cross-sectional nanodiffraction: A critical comparison. *J. Appl. Crystallogr.* **2013**, *46* (5), 1378–1385.
- (55) He, B. B. *Two-dimensional X-ray Diffraction*; Wiley, 2018.
- (56) Dailey, M.; Li, Y.; Printz, A. D. Residual Film Stresses in Perovskite Solar Cells: Origins, Effects, and Mitigation Strategies. *ACS Omega* **2021**, *6* (45), 30214–30223.
- (57) Rolston, N.; Bush, K. A.; Printz, A. D.; Gold-Parker, A.; Ding, Y.; Toney, M. F.; McGehee, M. D.; Dauskardt, R. H. Engineering Stress in Perovskite Solar Cells to Improve Stability. *Adv. Energy Mater.* **2018**, *8* (29), 1802139.
- (58) Wang, H.; Zhu, C.; Liu, L.; Ma, S.; Liu, P.; Wu, J.; Shi, C.; Du, Q.; Hao, Y.; Xiang, S.; et al. Interfacial Residual Stress Relaxation in Perovskite Solar Cells with Improved Stability. *Adv. Mater.* **2019**, *31* (48), No. e1904408.
- (59) Hoffman, R. W. Stresses in thin films: The relevance of grain boundaries and impurities. *Thin Solid Films* **1976**, *34* (2), 185–190.
- (60) Abermann, R.; Kramer, R.; Mäser, J. Structure and internal stress in ultra-thin silver films deposited on MgF₂ and SiO substrates. *Thin Solid Films* **1978**, *52* (2), 215–229.
- (61) Laugier, M. Intrinsic stress in thin films of vacuum evaporated LiF and ZnS using an improved cantilevered plate technique. *Vacuum* **1981**, *31* (3), 155–157.
- (62) Tamulevičius, S. Stress and strain in the vacuum deposited thin films. *Vacuum* **1998**, *51* (2), 127–139.
- (63) Spaepen, F. Interfaces and stresses in thin films. *Acta Mater.* **2000**, *48* (1), 31–42.
- (64) Cammarata, R. C.; Trimble, T. M.; Srolovitz, D. J. Surface stress model for intrinsic stresses in thin films. *J. Mater. Res.* **2000**, *15* (11), 2468–2474.
- (65) Floro, J. A.; Chason, E.; Cammarata, R. C.; Srolovitz, D. J. Physical origins of intrinsic stresses in Volmer-Weber thin films. *MRS Bull.* **2002**, *27* (1), 19–25.
- (66) Nix, W. D.; Clemens, B. M. Crystallite coalescence: A mechanism for intrinsic tensile stresses in thin films. *J. Mater. Res.* **1999**, *14* (8), 3467–3473.
- (67) Rajamani, A.; Sheldon, B. W.; Chason, E.; Bower, A. F. Intrinsic tensile stress and grain boundary formation during Volmer-Weber film growth. *Appl. Phys. Lett.* **2002**, *81* (7), 1204–1206.
- (68) Sheldon, B. W.; Lau, K. H. A.; Rajamani, A. Intrinsic stress, island coalescence, and surface roughness during the growth of polycrystalline films. *J. Appl. Phys.* **2001**, *90* (10), 5097–5103.
- (69) Chen, M.; Dong, Y.; Zhang, Y.; Zheng, X.; McAndrews, G. R.; Dai, Z.; Jiang, Q.; You, S.; Liu, T.; Harvey, S. P.; et al. Stress Engineering for Mitigating Thermal Cycling Fatigue in Perovskite Photovoltaics. *ACS Energy Lett.* **2024**, *9*, 2582–2589.
- (70) Zeiske, S.; Sandberg, O. J.; Zarrabi, N.; Wolff, C. M.; Raoufi, M.; Peña-Camargo, F.; Gutierrez-Partida, E.; Meredith, P.; Stolterfoht, M.; Armin, A. Static Disorder in Lead Halide Perovskites. *J. Phys. Chem. Lett.* **2022**, *13* (31), 7280–7285.
- (71) Ugur, E.; Ledinský, M.; Allen, T. G.; Holovský, J.; Vlk, A.; De Wolf, S. Life on the Urbach Edge. *J. Phys. Chem. Lett.* **2022**, *13* (33), 7702–7711.
- (72) Ledinsky, M.; Šchönfelková, T.; Holovský, J.; Aydin, E.; Hájková, Z.; Landová, L.; Neyková, N.; Fejfar, A.; De Wolf, S.

Temperature Dependence of the Urbach Energy in Lead Iodide Perovskites. *J. Phys. Chem. Lett.* **2019**, *10* (6), 1368–1373.